Acquisition, preprocessing, and reconstruction of ultralow dose volumetric CT scout for organ-based CT scan planning

Zhye Yin[a)]
Image Reconstruction Laboratory, GE Global Research, Niskayuna, New York 12309

Yangyang Yao
X-ray and CT Laboratory, GE Global Research, Shanghai 201203, China

Albert Montillo
Biomedical Image Processing Laboratory, GE Global Research, Niskayuna, New York 12309

Mingye Wu
X-ray and CT Laboratory, GE Global Research, Shanghai 201203, China

Peter M. Edic
CT, X-ray and Functional Imaging, GE Global Research, Niskayuna, New York 12309

Mannudeep Kalra
Thoracic and Cardiac Imaging, Massachusetts General Hospital, Boston, Massachusetts 02114

Bruno De Man
Image Reconstruction Laboratory, GE Global Research, Niskayuna, New York 12309

(Received 24 September 2014; revised 23 April 2015; accepted for publication 24 April 2015; published 14 May 2015)

Purpose: Traditionally, 2D radiographic preparatory scan images (scout scans) are used to plan diagnostic CT scans. However, a 3D CT volume with a full 3D organ segmentation map could provide superior information for customized scan planning and other purposes. A practical challenge is to design the volumetric scout acquisition and processing steps to provide good image quality (at least good enough to enable 3D organ segmentation) while delivering a radiation dose similar to that of the conventional 2D scout.
Methods: The authors explored various acquisition methods, scan parameters, postprocessing methods, and reconstruction methods through simulation and cadaver data studies to achieve an ultralow dose 3D scout while simultaneously reducing the noise and maintaining the edge strength around the target organ.
Results: In a simulation study, the 3D scout with the proposed acquisition, preprocessing, and reconstruction strategy provided a similar level of organ segmentation capability as a traditional 240 mAs diagnostic scan, based on noise and normalized edge strength metrics. At the same time, the proposed approach delivers only 1.25% of the dose of a traditional scan. In a cadaver study, the authors' pictorial-structures based organ localization algorithm successfully located the major abdominal-thoracic organs from the ultralow dose 3D scout obtained with the proposed strategy.
Conclusions: The authors demonstrated that images with a similar degree of segmentation capability (interpretability) as conventional dose CT scans can be achieved with an ultralow dose 3D scout acquisition and suitable postprocessing. Furthermore, the authors applied these techniques to real cadaver CT scans with a CTDI dose level of less than 0.1 mGy and successfully generated a 3D organ localization map. [http://dx.doi.org/10.1118/1.4921065]

Key words: 3D volumetric scout, ultralow dose, organ segmentation and localization, scan planning

1. INTRODUCTION

A 2D planning radiograph (referred to as scout, scanogram, or topogram) is a radiographic scan of a patient prior to a main diagnostic CT scan. 2D planning radiographs are used to assess patient centering and for planning the main diagnostic CT scan. CT vendors use the planning radiograph to adapt tube current for automatic exposure control techniques based on a user-specified image quality metric. These radiograph-based, automatic exposure control techniques are generally limited to tube current modulation according to geometric or attenuation asymmetries in the region of scanning. Like projection radiography, these 2D planning radiographs are also 2D projections of a 3D body anatomy. Although some anatomic landmarks such as lungs and bones can be identified on these planning radiographs, they are insufficient for accurate delineation or segmentation of most soft tissue organs or structures (such as liver, spleen, kidneys, and urinary bladder). The boundaries of these soft tissue organs are often difficult to identify due to the overlapping nature of tissue

projected onto a 2D planning radiograph, which can lead to unnecessary extra padding, high incidence of rescan, and variability among operators.

Automatic segmentation or extraction of organ boundaries for heart and lung from the 2D planning radiograph without user intervention has been explored before[1–3] to enhance organ position, but segmentation of adjacent soft tissue organs has proven to be very challenging. In this paper, we propose a 3D volumetric preparatory scan, i.e., 3D scout, to segment target organs for scan planning while delivering radiation dose similar to a conventional 2D scout. A 3D scout with a full organ map may enable other applications such as customized nonsinusoidal mA modulation,[4–6] automatic organ avoidance tube current modulation,[6–8] patient centroid estimation with better accuracy,[9] and organ dose reporting.[10] A 3D scout and its associated applications may have several potential benefits in clinical practice. First, it could provide more accurate patient information to avoid overscanning, rescanning, and unnecessary scanning in clinical practice. It could allow canceling the main exam when enough contraindications are observed in the 3D scout (metal, foreign object, size, etc.) to further protect patient from unnecessary radiation. Second, organ-based scan protocols for cardiology and liver oncology/dual energy are gaining a lot of attention where segmented/localized organ information is critical. Region of interest (ROI) scanning is also gaining interest in academia in the context of customized protocols for smaller organs such as the kidneys. Third, it can enable or improve organ dose modulation protocols, where the tube current of each view is specifically controlled to reduce the dose to radiosensitive organs such as the breasts.

The dose from a conventional 2D scout acquisition is a small fraction of the dose from the main scan, typically 0.4%–2%, depending on the protocol. For example, a typical shoulder region scan may use 300 mAs integrated tube current while a 2D scout acquisition is done at 4.5 mAs (or 1.5% of the main scan). The latter was computed assuming 10 and 80 mA for the anterior–posterior and lateral views, respectively, and 0.05 s total x-ray exposure time. Our goal is to achieve image quality sufficient for organ segmentation based on an ultralow dose 3D scout scan using a dose comparable to a conventional 2D scout scan. Reconstructed images from such a low dose acquisition may show degradation due to high noise and image artifacts such as streaks and azimuthal blur depending on the mode of acquisition, which makes conventional edge and region based image segmentation methods[11,12] yield low segmentation accuracy.[13–15] More advanced model-based organ segmentation (MBS) methods hold greater potential to overcome some of these challenges; however, even these can fail when the noise or streaks are prominent.[16–18]

In this work, we explored various ultralow dose acquisition, preprocessing, and reconstruction strategies to reduce the radiation dose of a 3D scout while maintaining appropriate image quality to produce a volumetric organ map. To evaluate each strategy, we first defined a new image quality metric to reflect organ "segmentability" (i.e., the ability to segment), rather than using a specific segmentation approach. As a result, our experiments are largely independent of the specific organ segmentation algorithm implementation. We focused on the abdomen region, specifically the liver, which is one of the most challenging organs due to its shape, complexity, intersubject variability, and low boundary contrast at its inferior aspect. Our methodology can also be extended to other regions and organs.

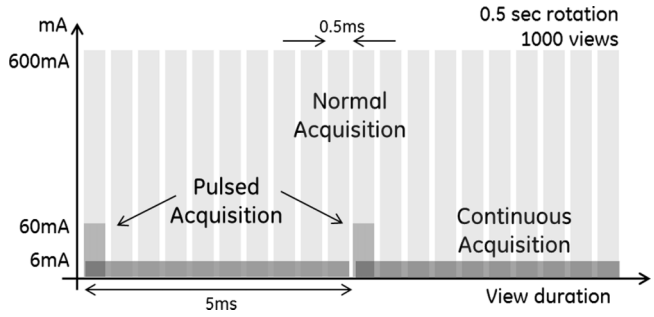

FIG. 1. 3D scout acquisition strategy: (a) normal acquisition, (b) pulsed acquisition, and (c) continuous-exposure acquisition. Gaps between views illustrate DAS reading while incurring electronic noise.

Second, we simulated each 3D scout acquisition strategy using CATSIM (Ref. 19) with the anthropomorphic xCAT phantom.[20] For simplicity, we used a third-generation axial scan mode with eight detector rows, positioned over the liver region. We used a variety of preprocessing and reconstruction strategies to generate 3D scout images. Finally, we analyzed the image quality of various 3D scout strategies visually and based on organ segmentability and noise metrics. We also applied the proposed 3D scout strategy to a cadaver data set scanned at Massachusetts General Hospital (MGH) and evaluated the performance of a pictorial-structures based, multiorgan localization algorithm.[21,22]

2. 3D SCOUT STRATEGY

2.A. Acquisition

To achieve an ultralow dose 3D scout acquisition, radiation from the x-ray tube can be reduced by using lower tube voltage (kVp) and lower tube current (mA). Exposure time can also be minimized to further reduce the dose. We previously performed a simulation study of sparse-view acquisitions, in which fewer views are taken during rotation, resulting in a smaller total exposure time.[23]

A sparse-view acquisition can be implemented by tube pulsing, where an x-ray source is turned on and off during rotation. However, the latest commercial CT scanners do not support fast pulsed acquisitions due to limitations of the x-ray generation hardware. Therefore, we propose a continuous-exposure acquisition where the x-ray source remains on during rotation but fewer views are acquired per rotation, as shown in Fig. 1(c). For example, if a normal acquisition is performed with 600 mA, 1000 views, and 0.5 ms exposure times per view, then the pulse acquisition of 1% of the original dose would be done with 60 mA, 100 views, and 0.5 ms exposure times per view. On the other hand, the continuous-exposure acquisition of 1% of the original dose

would be done with 6 mA, 100 views, and 5 ms exposure times, as shown in Fig. 1. The total number of photons per view shows that the photon noise and electronic noise would be similar for both pulsed acquisition and continuous-exposure acquisition since the exposure time is longer in the continuous-exposure acquisition and the electronic noise per view is approximately independent of the integration time. Furthermore, a continuous-exposure acquisition can easily be implemented in current commercial CT scanners by updating the control software.

Pulsed acquisitions and continuous-exposure acquisitions will still produce different artifacts in a 3D scout. A sparse-view pulsed acquisition with a simple filtered back projection (FBP) will produce more streaks, which will be exacerbated for objects with high attenuation. On the other hand, a sparse-view continuous-exposure acquisition will have more azimuthal blur than a sparse-view pulsed acquisition. This will appear as rotational smoothing that increases with the distance from the rotation axis.

2.B. Preprocessing

The main purpose of a 3D scout is to segment organs for organ-based CT scan planning, for example, a heart for cardiac protocols and a liver for liver protocols. Also for other usages of a 3D scout, such as aggressive mA modulation or patient centroid estimation, the spatial resolution requirement is much lower than for diagnostic CT scans. Since the main concern for a 3D scout acquisition is to minimize the impact of photon noise and electronic noise at very low integrated tube currents, i.e., on the order of a few mAs, we proposed to trade-off spatial resolution for noise performance by smoothing data before reconstruction. We tested three different approaches. First, detector cells are merged into larger detector cells, in groups of 2×2 or 3×3. Second, instead of taking a simple average, we can compute the trimmed mean of the central 80% of the sinogram values in each neighborhood. Finally, a 2D Gaussian smoothing filter can be applied, empirically tuned to match the noise reduction power of the first (rebinning) method. For the clinical data processing, we applied only the trimmed mean filter.

2.C. Reconstruction

A 3D scout is a preparatory scan, which is processed before the main scan is acquired. Since the patient remains in the scanner, there is a time constraint on the reconstruction and processing of the 3D scout. Full model-based iterative reconstruction approaches have been very successful in handling ultralow dose and sparse acquisitions,[24,25] but can require long computation times. Other iterative reconstruction approaches, such as ASIR,[26] have high noise reduction capability and operate in real time without minimal computing hardware. Rather than focusing on a specific iterative reconstruction technique, we emulated its impact by reducing the noise. We used FBP reconstruction with a commercially available smooth reconstruction kernel and averaged multiple noise realizations to emulate the impact of iterative reconstruction. We applied view interpolation to minimize streak artifacts from the sparse-view nature of the data.

3. EXPERIMENTS

We designed multiple experiments to evaluate various 3D scout strategies, as summarized in Tables I and II. Experiment 1 uses an extra high dose, extra low noise acquisition and was used to establish the ground truth boundary of a target organ. Experiment 2 uses a standard diagnostic CT acquisition protocol with normal dose and noise levels (240 mAs with 120 kVp) and serves as the baseline. Experiments 3–8 consist of pulsed acquisition protocols with different levels of sparseness, tube current, and corresponding dose levels. The lowest-dose experiment was also preprocessed with detector rebinning (Experiments 9–10), reconstructed with a smoother kernel (Experiment 11), reconstructed with emulated iterative reconstruction (Experiment 12), and processed with combinations of the above (Experiments 13–14).

The effect of iterative reconstruction was emulated by averaging four FBP images from different noise realization simulations, resulting in about 50% reduction in noise while maintaining resolution, which is what we would expect from advanced real-time iterative reconstruction techniques.

Experiments 15–17 have continuous x-ray exposure but reduce the number of views by increasing the view time. The dose percentage was computed by dividing the mAs of a given strategy by 240 mAs, which was the base line of a standard scan.

In a second series of experiments (Table II), we repeated the ground truth (Experiment 1) and the baseline (Experiment 2) and we extended the first set of experiments to include several low dose acquisition protocols with standard processing (Experiments 3–6). The tube current of the various continuous-exposure acquisition strategy went down further from 60 to 7.5 mA while the view exposure time increased from 0.4 to 3.2 ms while maintaining the same x-ray tube output (Experiments 4–6).

Experiments 7–10 were further processed with detector Gaussian blurring. The Gaussian blurring filter was designed to replicate a 3×3 detector rebinning. In Experiments 11–18, we replaced the standard filtered backprojection to reconstruct a sparse-view acquisition (12.5% of standard number of views) by a linear view interpolation to upsample the data prior to filtered backprojection.

We simulated all 3D scout acquisition strategies shown in Tables I and II using CATSIM (Ref. 19) with the anthropomorphic xCAT phantom[20] including both photon and electronic noise models, which were validated against a GE VCT scanner. A third-generation axial acquisition mode was used for simplicity. A total of eight rows of detectors were positioned over the liver region. The central slice was reconstructed with a standard 3D filtered backprojection and the proposed variations, using a voxel size of $1\times1\times0.625$ mm and a field of view of 360 mm. The size of the xCAT phantom at the liver level was roughly 300×250 mm.

TABLE I. Experiment parameters for various acquisition and processing strategies.

Experiment	Tube current (mA)	Tube output (mAs)	Acquisition number of views	Exposure time per view (ms)	Dose from base line (%)	Reconstruction number of views	Note
			Ground-truth and baseline				
1	2000	800	1000	0.4	333	1000	Ground truth
2	600	240	1000	0.4	100	1000	Base line
			Pulsed acquisition—standard processing				
3	240	24	250	0.4	10	250	Pulsed acquisition
4	240	12	125	0.4	5	125	Pulsed acquisition
5	120	12	250	0.4	5	250	Pulsed acquisition
6	120	6	125	0.4	2.5	125	Pulsed acquisition
7	60	6	250	0.4	2.5	250	Pulsed acquisition
8	60	3	125	0.4	1.25	125	Pulsed acquisition
			Pulsed acquisition—advanced processing				
9	60	3	125	0.4	1.25	125	Detector rebinning (2×2)
10	60	3	125	0.4	1.25	125	Detector rebinning (3×3)
11	60	3	125	0.4	1.25	125	Smooth kernel
12	60	3	125	0.4	1.25	125	Real-time iterative reconstruction
13	60	3	125	0.4	1.25	125	Kernel + rebinning (3×3)
14	60	3	125	0.4	1.25	125	Kernel + rebinning (3×3) + iteration
			Continuous acquisition—advanced processing				
15	60	12	250	0.8	5	250	Kernel + rebinning (3×3) + iteration
16	60	6	125	0.8	2.5	125	Kernel + rebinning (3×3) + iteration
17	60	3	62	0.8	1.25	62	Kernel + rebinning (3×3) + iteration

Finally, the most promising 3D scout strategy from this simulation study was applied to a cadaver data set acquired at MGH, Boston, MA. This cadaver was originally scanned using a helical protocol of 30 mAs and 120 kVp, reporting a CTDI of 0.9 mGy. We emulated the pulsed sparse acquisition by dropping 90% of the views to achieve an ultralow dose 3D scout CTDI of 0.09 mGy. These data were processed with a trimmed mean filter (20% trim) and a quadratic

TABLE II. Experiment parameters for various 3D strategies with continuous-exposure acquisition.

Experiment	Tube current (mA)	Tube output (mAs)	Acquisition number of views	Exposure time per view (ms)	Dose from base line (%)	Reconstruction number of views	Note
			Standard processing techniques				
1	2000	800	1000	0.4	333	1000	Ground truth
2	600	240	1000	0.4	100	1000	Base line
3	60	3	125	0.4	1.25	125	Pulsed acquisition
4	30	3	125	0.8	1.25	125	Continuous-exposure acquisition
5	15	3	125	1.6	1.25	125	Continuous-exposure acquisition
6	7.5	3	125	3.2	1.25	125	Continuous-exposure acquisition
			Noise reduction techniques				
7	60	3	125	0.4	1.25	125	Gaussian detector blur
8	30	3	125	0.8	1.25	125	Gaussian detector blur
9	15	3	125	1.6	1.25	125	Gaussian detector blur
10	7.5	3	125	3.2	1.25	125	Gaussian detector blur
			Aliasing reduction techniques				
11	60	3	125	0.4	1.25	250	+ View interpolation (upsampled to 250)
12	30	3	125	0.8	1.25	250	+ View interpolation (upsampled to 250)
13	15	3	125	1.6	1.25	250	+ View interpolation (upsampled to 250)
14	7.5	3	125	3.2	1.25	250	+ View interpolation (upsampled to 250)
15	60	3	125	0.4	1.25	500	+ View interpolation (upsampled to 500)
16	30	3	125	0.8	1.25	500	+ View interpolation (upsampled to 500)
17	15	3	125	1.6	1.25	500	+ View interpolation (upsampled to 500)
18	7.5	3	125	3.2	1.25	500	+ View interpolation (upsampled to 500)

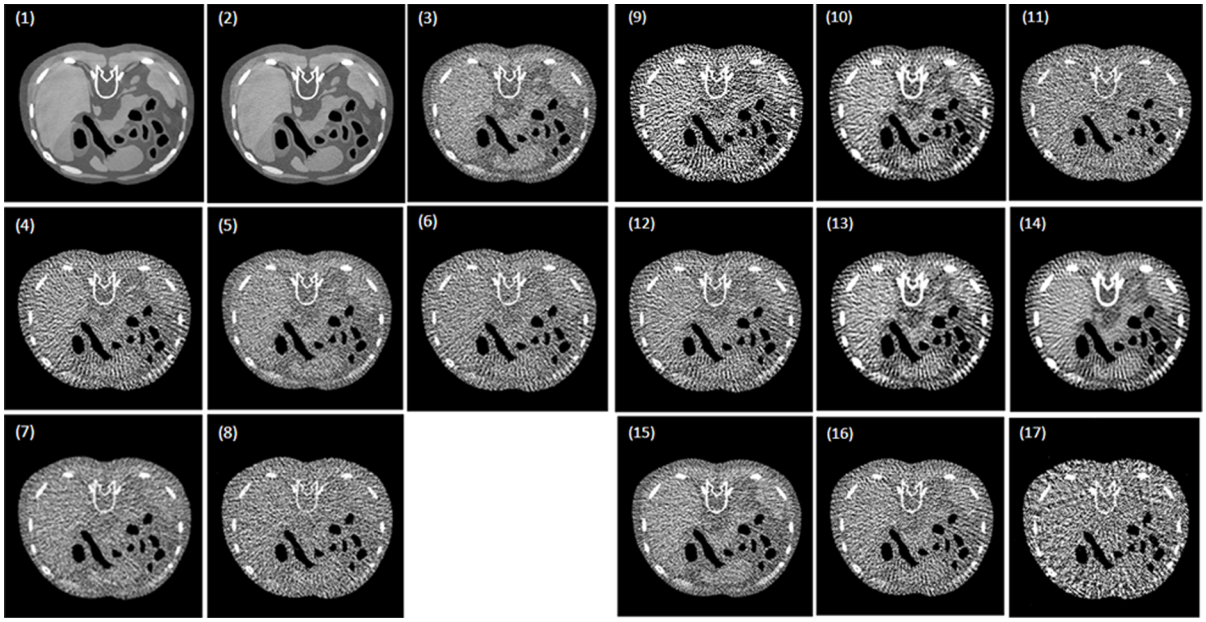

FIG. 2. 3D scout with various acquisitions, preprocessing, and reconstruction techniques is shown. Images are from (1) ground truth, (2) standard dose level, (3)–(8) various low dose level, ranging from 24 to 3 mAs with pulsed acquisition, (9)–(10) 2×2 or 3×3 detector rebinning, (11) smooth FBP kernel, (12) real-time iterative reconstruction emulation, (13) combination of 3×3 rebinning and smooth kernel, (14) combination of 3×3 rebinning, smooth kernel, and iterative reconstruction emulation, and (15)–(17) various continuous acquisition protocols with proposed preprocessing techniques. See Table I for details.

view interpolation and were reconstructed with a standard helical reconstruction algorithm. A pictorial-structures based multiorgan localization algorithm[21,22] was applied to the fully processed 3D scout image volume to generate the bounding box of major organs such as the heart, lungs, liver, and kidneys.

4. RESULTS AND DISCUSSION

We evaluated the images from the various 3D scout strategies by visual inspection, based on the image quality metrics, and by applying an automated organ localization algorithm. Shown in Fig. 2 are the baselines and various

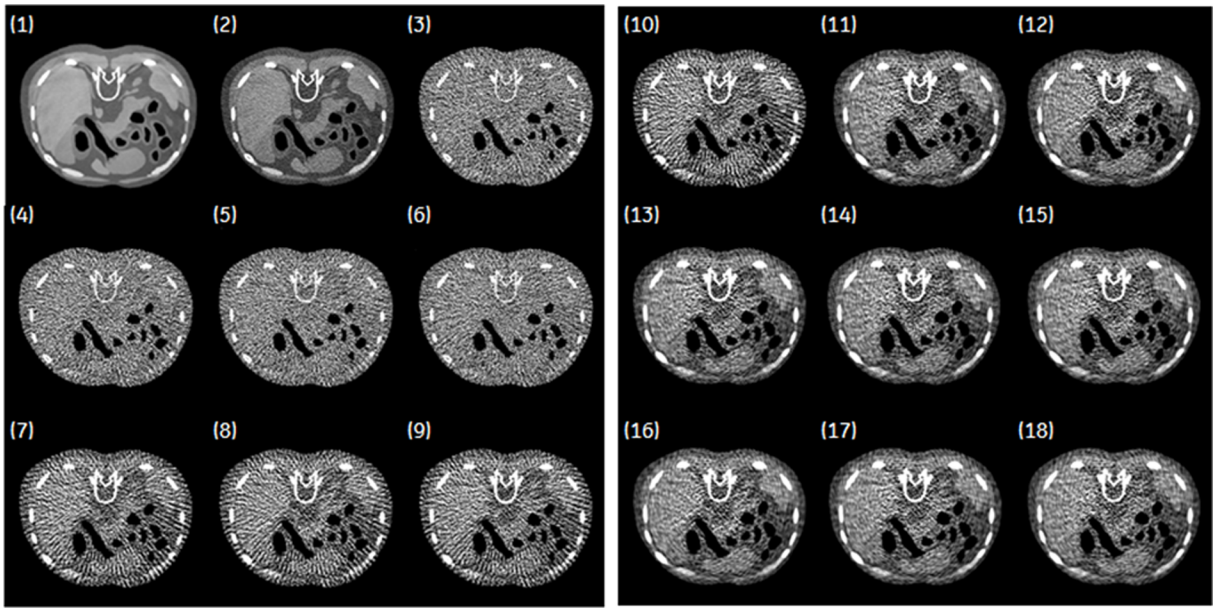

FIG. 3. 3D scout with various acquisitions, preprocessing, and reconstruction techniques is shown. Images are from (1) ground truth, (2) standard dose level, (3) pulse acquisition, (4)–(6) various continuous acquisition protocols with different view exposure times at 3 mAs dose level, (7)–(10) Gaussian blur on (4)–(6) acquisitions, (11)–(14) view upsampling by two combined with Gaussian blur, and (15)–(18) view upsampling by four combined with Gaussian blur. See Table II for details.

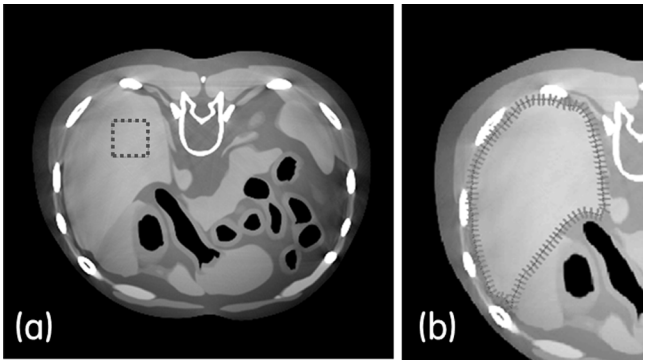

FIG. 4. (a) Noise metric: 2×2 cm rectangular ROI in the liver region with a dotted line. (b) NES metric: interpolated ground truth contour, $c(t)$, and perpendicular line segments, $s(r)$.

3D scout images from various acquisitions, preprocessing, and reconstruction strategies from Table I. Qualitatively, we observe that, as the tube current and number of views drop, images rapidly lose soft tissue contrast and the boundary of the liver becomes invisible, as shown in Figs. 2(6)–2(8). Images with a combination of various denoising techniques resulted in noisy, but more visible organ boundaries. The images processed with the combination of a 3×3 window detector rebinning, a smooth reconstruction kernel, and iterative reconstruction emulation [Experiment 14 in Table I, shown in Fig. 2(14)] show a well-defined liver boundary while delivering only a fraction (1.25%) of the dose relative to the baseline [Experiment 2 in Table I, Fig. 2(2)]. However, streak artifacts from the pulsed acquisition with a FBP-based sparse reconstruction are very pronounced, as shown in Figs. 2(9)–2(14).

Furthermore, we compared Experiment 14 (which has twice the number of views as Experiment 17) and Experiment 17 (which has twice the exposure time of Experiment 14) with the same mA level, in order to assess the impact of having fewer views with longer exposure time. However, we observed that images reconstructed without a dedicated sparse-view reconstruction algorithm have very high noise and invisible organ boundaries, as shown in Fig. 2(17).

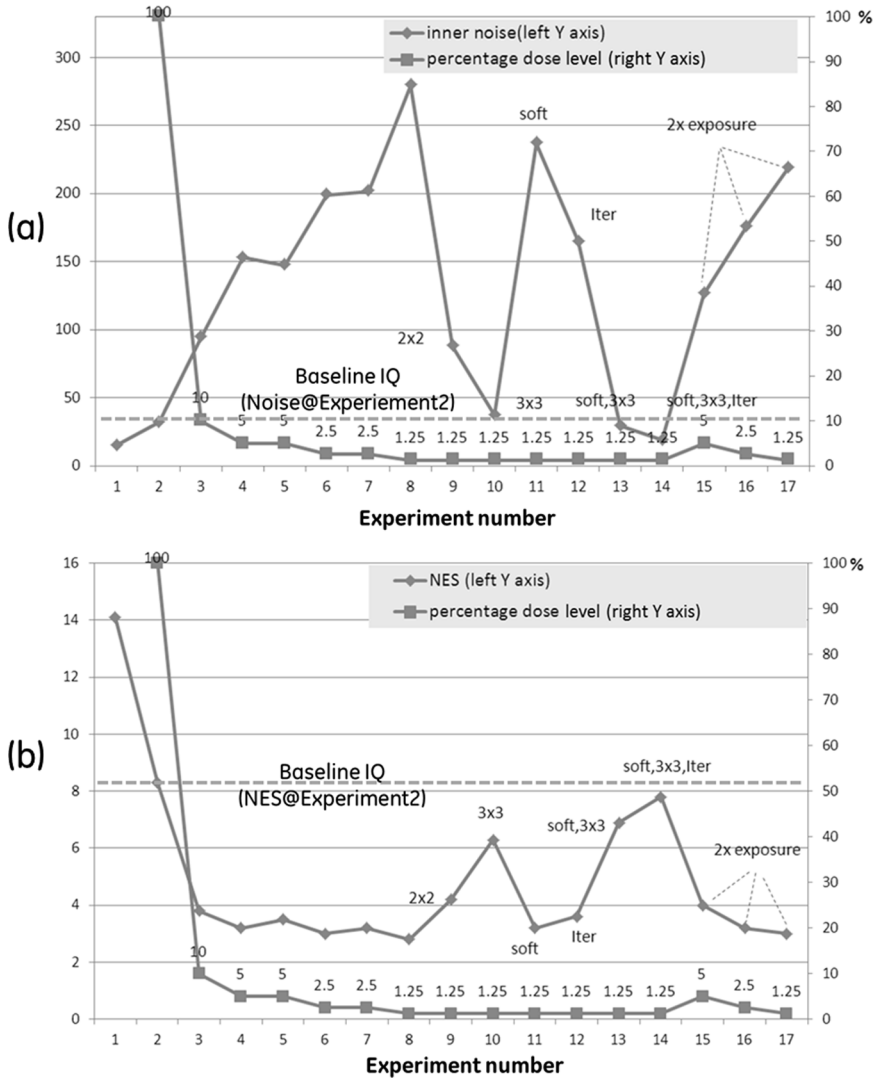

FIG. 5. (a) Noise and (b) NES metrics from cases in Table I are shown in diamonds and the percentage dose from the baseline (Experiment 2) is shown in squares. The dashed horizontal lines represent noise and NES metric of the reference case, Experiment 2.

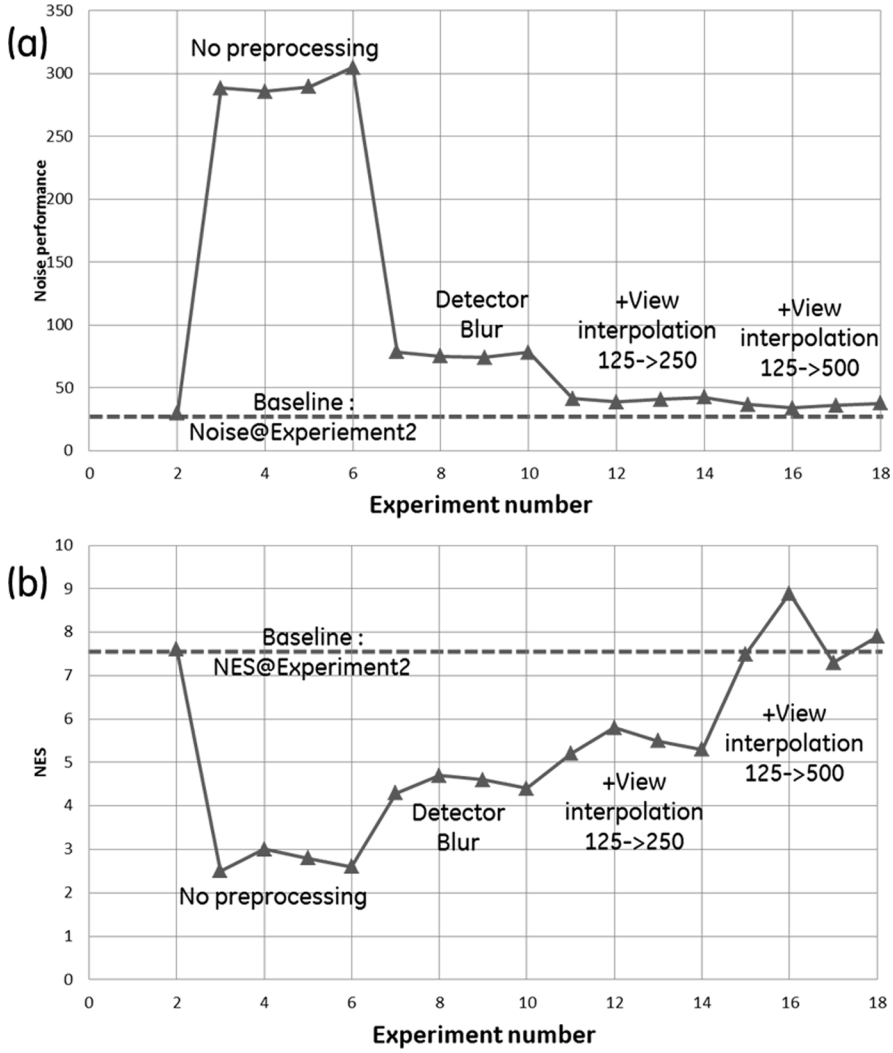

FIG. 6. (a) Noise and (b) NES metrics from cases in Table II are shown as a solid line. Dashed horizontal lines represent noise and NES metrics of the reference case, Experiment 2.

Additional 3D scout images from the second set of experiments of Table II are shown in Fig. 3. The continuous-exposure acquisitions with varying view exposure times show similar noise level when the tube output (mAs) was kept the same [see Figs. 3(4)–3(6)]. Applying a Gaussian detector blur effectively reduces the noise and enhances the contrast, but reveals radial streak artifacts due to the sparse acquisition [see Figs. 3(7)–3(10)]. We applied additional view interpolation which helped reduce streak artifacts; however, the azimuthal blur manifested as short arcs in the rotation direction and nonuniform noise levels. This can be clearly seen in Figs. 3(11)–3(18), where the central region shows more noise than the peripheral region.

To further assess the proposed 3D scout strategy, we devised two image quality metrics for organ segmentability to compare various 3D scout strategies in this simulation study. The first metric measures the noise at the interior portion of the liver using a 2×2 cm rectangular ROI, as shown by the dotted box in Fig. 4(a).

The organ interior noise, σ, is the standard deviation of voxel intensities from a ROI in the liver interior,

$$\sigma = \text{stdev}(\text{rectangular ROI}). \quad (1)$$

The success of organ segmentation from an ultralow dose 3D scout scan is highly dependent on the contrast changes along the boundary of the organ. High frequency artifacts such as streaks, increased noise, and blurred boundaries due to heavy postprocessing can impair the success of organ segmentation. Therefore, to measure the strength of the contrast change at the boundary, we propose a new metric, normalized edge strength (NES), which normalizes existing edge strength metrics.[27] A clearly defined edge will have a high intensity gradient perpendicular to the boundary and a low gradient parallel to the boundary. To determine parallel gradient and perpendicular gradient, we manually extract the ground truth boundary from the liver in the reconstructed image of the xCAT phantom using VV 4D slicer.[28] This boundary is represented by a piecewise linear polygonal curve [shown in Fig. 4(b)]. The intensity profile along the organ boundary curve, i.e., parallel to the curve, is defined as $c(t)$ which can be parameterized by t, the arc length along c.

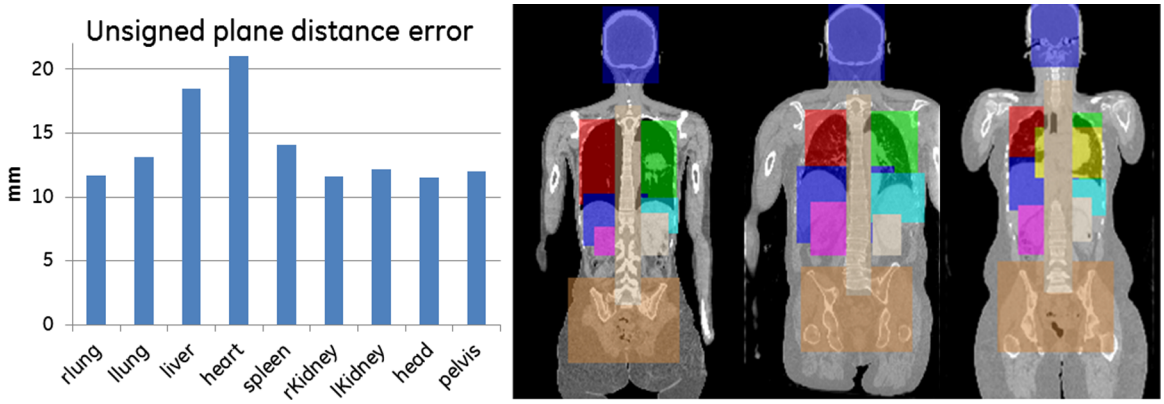

FIG. 7. Organ localization results. Left: Accuracy of the pictorial-structures based organ localization algorithm measured as the mean distance error. Right: As shown in these three different subjects of varying anatomical proportions, the organ localization algorithm (Ref. 21) produces visually accurate results. The automatically identified organs include the head, pelvis, spine, heart, lungs, kidneys, liver, and spleen.

To measure the perpendicular gradient, we evenly distribute 7 mm long line segments that straddle and are perpendicular to the boundary [shown in Fig. 4(b)]. The image intensity profiles along these line segments are denoted as $s(r)$ in which r parametrizes the arc length along s. Finally, we define the NES of a boundary as

$$\mathrm{NES} = \frac{\mathrm{trimmean}\left(\left\{\max\left|\frac{ds_i(r)}{dr}\right|\right\}_{i=1}^{N},5\right)}{\mathrm{trimmean}\left(\left\{\left|\frac{dc(t)}{dt}\right|\right\},5\right)}. \quad (2)$$

For robustness to outliers, instead of taking an average of all the computed gradients, we first trimmed the highest and the lowest 2.5% values. For a vector input v, the trimmean $(v,5)$ function computes the mean of elements in v, excluding the highest and lowest 2.5% values.

To quantitatively assess the performance of various 3D scout strategies, we computed the noise metric and NES metric for every case in Tables I and II. For the experiments in Table I, the combination of detector rebinning, smooth reconstruction kernel, and iterative reconstruction emulation (Experiment 14) improves the NES and noise performance and achieves a similar image quality level compared to the full dose acquisition (Experiment 2), as shown in Fig. 5. The noise and NES metrics for each strategy are marked with diamond symbols in Figs. 5(a) and 5(b), respectively, while the dose percentage relative to the baseline (Experiment 2) is marked with square markers.

The horizontal lines represent image quality metric values from the baseline case (Experiment 2).

For the additional experiments in Table II in which the tube outputs are equal for every strategy (3 mAs or 1.25% of the baseline tube output), the combination of Gaussian blur in projection domain and 500 view upsampling through interpolation (Experiments 15–18) provides the most improvement in the noise and NES metrics, shown in Fig. 6(b). Note that the level of improvement is on par

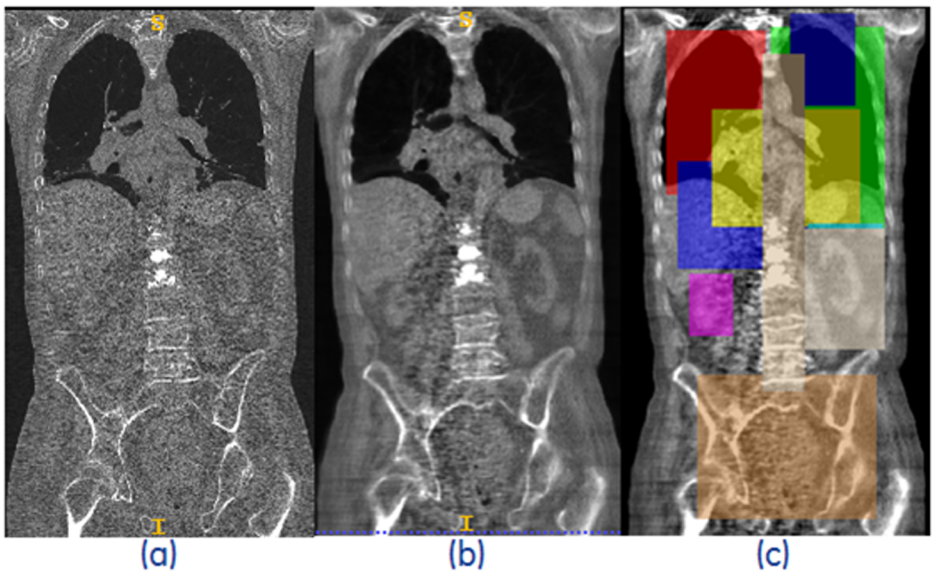

FIG. 8. Reconstructed images and organ localization. (a) Coronal slice from original cadaver data acquired at 0.9 mGy, (b) 0.09 mGy equivalent version of the same slice after noise reduction, and (c) located organ bounding boxes, including lungs in red and green.

with the experiments from Table I, but do not use iterative reconstruction emulation. Noise and NES metrics are marked with triangle markers in Figs. 6(a) and 6(b), respectively. The dashed horizontal lines indicate the baseline (Experiment 2).

Finally, to evaluate our proposed 3D scout acquisition and analysis approach, we applied a simulation study to the clinical data acquired at MGH, Boston, MA. In this study, we begin by applying a pictorial-structures based multiorgan, machine learning-based localization algorithm.[21,22] We trained the method with more than 30 subjects of low resolution CT data from a PET/CT/MR trimodality imaging study at University Hospital Zurich, Switzerland, which has a similar image quality to the processed 3D scout. The accuracy of the organ localization algorithm was measured by the unsigned, perpendicular planar distance error in mm between the ground truth locations of the organs' bounding box sides and their detected locations. The mean distance error ranged from 10 to 20 mm, as shown in Fig. 7, which is adequate for the scan planning and organ-based mA modulation application. The trained organ localizer was then applied to the fully processed 3D scout image volumes from the cadaver data sets to generate the 3D organ bounding boxes. Examples of organ bounding box localization results for the heart, lungs, liver, and kidneys are shown in Fig. 8. The reconstructed coronal slice of the original data acquired at 0.9 mGy is shown in Fig. 8(a). We further dropped 90% of views and applied trimmed mean filter and view interpolation, shown in Fig. 8(b). Finally, we extracted the bounding boxes of heart, lungs, liver, kidneys, and pelvis, shown in Fig. 8(c). Since the standard CTDI for chest-abdomen-pelvis protocol is 10–15 mGy, the proposed 3D scout strategy successfully demonstrates segmentability at less than 1% of the dose relative to the baseline protocol. Currently, the accuracy of the bounding box is ~10–20 mm depending on the organ[21] and further segmentation of the organ from the initial bounding box solution will further improve accuracy.[2,3]

5. CONCLUSION

We investigated the feasibility of acquiring an ultralow dose 3D scout and providing sufficient image quality to generate 3D volumetric organ localizations for subsequent scan planning. We achieved low dose by reducing tube voltage and tube current while acquiring sparse views and maintaining the total number of x-ray photons per view using sparse-view, either pulsed or continuous-exposure acquisitions. We also proposed additional reconstruction and postprocessing approaches to improve the image quality. We defined two image quality metrics to measure the edge strength at the boundary and noise level inside of organs. In our study we applied this to the liver to compare the "segmentability" of images produced by various acquisition and processing methods. In a simulation study, we successfully demonstrated that the 3D scout delivers a similar degree of organ localization capability as a regular 240 mAs diagnostic scan while delivering only 1.25% of the radiation dose. Furthermore, we demonstrated the potential for the proposed 3D scout strategy on real clinical data and produced a reasonable 3D volumetric organ map with clinically relevant organs. In the future, we will demonstrate the preferred mode for a 3D scout acquisition in a clinical system and we will optimize preprocessing and reconstruction techniques to balance the azimuthal blur from view interpolation and streaks from sparse-view FBP reconstruction. Finally, we will investigate and quantify the benefit of the 3D scout in multiple scan planning and exposure control applications.[6]

ACKNOWLEDGMENTS

The authors of this paper are grateful for the help provided by Tosha Churchill and Paul Fitzgerald in editing and proofreading.

[a]Author to whom correspondence should be addressed. Electronic mail: yin@ge.com

[1]Y. Tao, Z. Peng, A. Krishnan, and X. Zhou, "Robust learning-based parsing and annotation of medical radiographs," IEEE Trans. Med. Imaging **30**(2), 338–350 (2011).

[2]A. Montillo, Q. Song, X. Liu, and J. Miller, "Parsing radiographs by integrating landmark set detection and multi-object active appearance models," Proc. SPIE **8669**, 86690H (2013).

[3]Q. Song, A. Montillo, R. Bhagalia, and V. Srikrishnan, "Organ localization using joint AP/LAT view landmark consensus detection and hierarchical active appearance models," in *Proceedings of Medical Computer Vision Workshop, Medical Image Computing and Computer-Assisted Intervention* (MICCAI), 2013.

[4]M. Gies, W. A. Kalender, H. Wolf, and C. Suess, "Dose reduction in CT by anatomically adapted tube current modulation: I. Simulation studies," Med. Phys. **26**, 2235–2247 (1999).

[5]W. A. Kalender, H. Wolf, and C. Suess, "Dose reduction in CT by anatomically adapted tube current modulation: II. Phantom measurements," Med. Phys. **26**, 2248–2253 (1999).

[6]Y. Jin, Z. Yin, Y. Yao, H. Wang, M. Wu, M. Kalra, and B. De Man, "Patient specific tube current modulation for CT dose reduction," Proc. SPIE **9412**, 94122Z (2015).

[7]S. V. Vollmar and W. A. Kalender, "Reduction of dose to the female breast in thoracic CT: A comparison of standard-protocol, bismuth-shielded, partial and tube-current-modulated CT examinations," Eur. Radiol. **18**(8), 1674–1682 (2008).

[8]J. Wang, X. Duan, J. A. Christner, S. Leng, K. L. Grant, C. H. McCollough, and B. Shielding, "Organ-based tube current modulation, and global reduction of tube current for dose reduction to the eye at head CT," Radiology **262**(1), 191–198 (2012).

[9]T. Toth, Z. Ge, and M. P. Daly, "The influence of patient centering on CT dose and image noise," Med. Phys. **34**, 3093–3101 (2007).

[10]J. A. Christner, J. M. Kofler, and C. H. McCollough, "Estimating effective dose for CT using dose–length product compared with using organ doses: Consequences of adopting international commission on radiological protection publication 103 or dual-energy scanning," Am. J. Roentgenol. **194**, 881–889 (2010).

[11]L. G. Shapiro and G. C. Stockman, *Computer Vision* (Prentice-Hall, New Jersey, 2001), pp. 279–325.

[12]R. C. Gonzalez and R. E. Woods, *Digital Image Processing*, 2nd ed. (Prentice Hall, New Jersey, 2002).

[13]S. Seifert, A. Barbu, S. Zhou, D. Liu, J. Feulner, M. Huber, M. Suehling, A. Cavallaro, and D. Comaniciu, "Hierarchical parsing and semantic navigation of full body CT data," Proc. SPIE **7259**(02), 1–8 (2009).

[14]V. Potesil, T. Kadir, G. Platsch, and M. Brady, "Personalization of Pictorial Structures for Anatomical Landmark Localization," in *IPMI* (Springer, New York, NY, 2011), pp. 333–345.

[15]S. Zhang, Y. Zhan, M. Dewan, J. Huang, D. Metaxas, and X. Zhou, "Deformable segmentation via sparse shape representation," in *Medical*

Image Computing and Computer-Assisted Intervention–MICCAI (Springer-Verlag, Berlin, 2011), pp. 451–458.
[16]T. F. Cootes, C. J. Taylor, D. H. Cooper, and J. Graham, "Active shape models–their training and application," Comput. Vision Image Understanding **61**(1), 38–59 (1995).
[17]S. C. Mitchell, J. G. Bosch, B. P. F. Lelieveldt, R. J. van der Geest, J. H. C. Reiber, and M. Sonka, "3-d active appearance models: Segmentation of cardiac MR and ultrasound images," IEEE Trans. Med. Imaging **21**(9), 1167–1178 (2002).
[18]T. F. Cootes, G. J. Edwards, and C. J. Taylor, "Active appearance models," in *European Conference on Computer Vision* (Springer-Verlag, Berlin, 1998), Vol. 2, pp. 484–498.
[19]B. De Man *et al.*, "CatSim: A new computer assisted tomography simulation environment," Proc. SPIE **6510**, 65102G (2007).
[20]W. P. Segars, M. Mahesh, T. J. Beck, E. C. Frey, and B. M. Tsui, "Realistic CT simulation using the 4D XCAT phantom," Med. Phys. **35**, 3800–3808 (2008).
[21]A. Montillo, Q. Song, B. Das, and Z. Yin, "Hierarchical pictorial structures for simultaneously localizing multiple organs in volumetric pre-scan CT," Proc. SPIE **9413**, 94130T (2015).
[22]X. Liu, Q. Song, P. Mendonca, X. Tao, and R. Bhotika, "Organ labeling using anatomical model-driven global optimization," in *First IEEE International Conference on Healthcare Informatics, Imaging and Systems Biology (HISB)* (IEEE, San Jose, CA, 2011), pp. 338–345.
[23]Y. Long, L. Cheng, X. Rui, B. De Man, A. Alessio, E. Asma, and P. Kinahan, "Analysis of ultra-low dose CT acquisition protocol and reconstruction algorithm combinations for PET attenuation correction," in *Proceeding of the 12th International Meeting on Fully Three-Dimensional Image Reconstruction in Radiology and Nuclear Medicine* (Fully 3D, Lake Tahoe, CA, 2013), pp. 400–403.
[24]A. P. J. Pickhardt, M. G. Lubner, D. H. Kim, J. Tang, J. A. Ruma, A. M. del Rio, and G.-H. Chen, "Abdominal CT with model-based iterative reconstruction (MBIR): Initial results of a prospective trial comparing ultralow-dose with standard-dose imaging," Am. J. Roentgenol. **199**(6), 1266–1274 (2012).
[25]E. Y. Sidky, C.-M. Kao, and X. Pan, "Accurate image reconstruction from few-views and limited-angle data in divergent-beam CT," J. X-Ray Sci. Technol. **14**(2), 119–139 (2006).
[26]P. Prakash, M. K. Kalra, S. R. Digumarthy, J. Hsieh, H. Pien, S. Singh, M. D. Gilman, and O. S. Jo-Anne, "Radiation dose reduction with chest computed tomography using adaptive statistical iterative reconstruction technique: Initial experience," J. Comput. Assisted Tomogr. **34**(1), 40–45 (2010).
[27]A. Montillo, J. Udupa, L. Axel, and D. Metaxas, "Interaction between noise suppression and inhomogeneity correction in MRI," Proc. SPIE **5032**, 1025–1036 (2003).
[28]VV-4D slicer, an open source image tool available from http://www.creatis.insa-lyon.fr/rio/vv/.